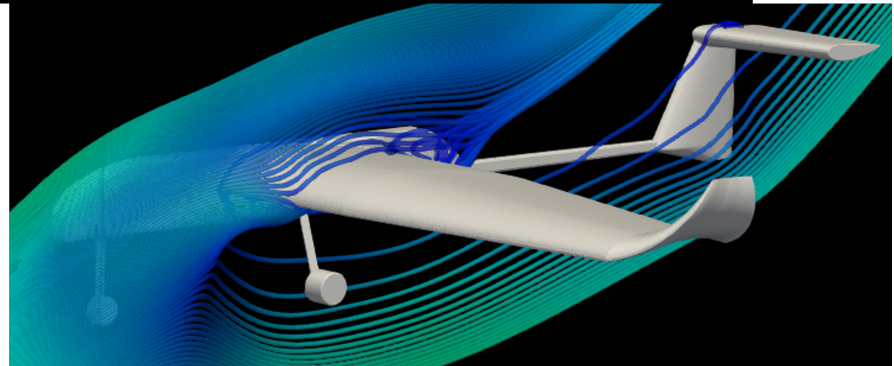
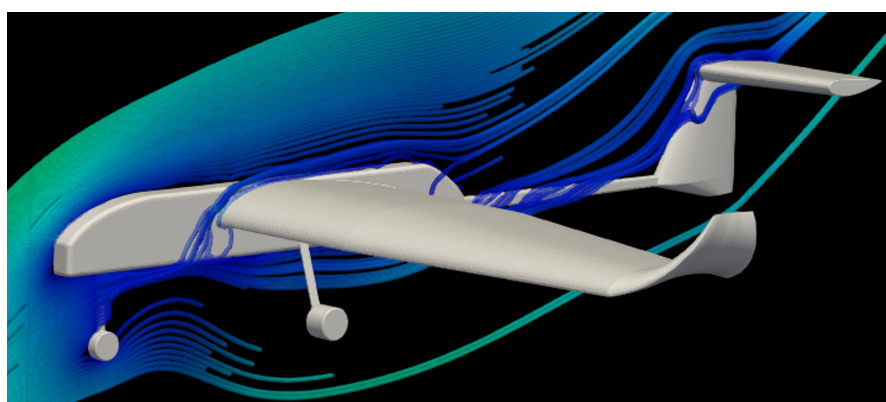
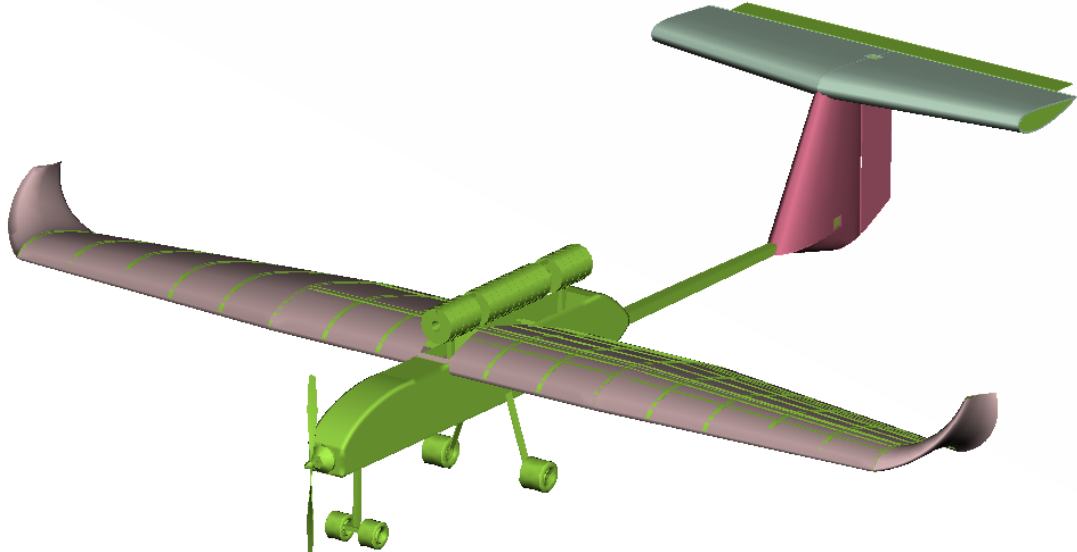


Aerodynamic Analysis of Aircraft using RANS CFD

Abhishek Dhiman (abhdh352)

Examiner: Roland Gardhagen



Abstract

The study is focused on the aerodynamics analysis of an Remote Controlled (RC) aircraft that was constructed for the SAE Brazil competition with certain design constraints in design parameters, material, and electronic components. The test flights resulted in crash landings which motivated the detailed aerodynamic analysis using Computational Fluid Dynamics (CFD) simulation approach with recommended best practises to analyze performance expectation from the salient geometric features like T-tail configuration, multi-planform wing, inverted horizontal stabilizer, etc at various Angle of Attack (AoA). The input was a detailed CAD model from the conceptual design phase that called for multiple stages i.e. Computer-Aided Design (CAD) cleaning, solution, and post-processing for the detailed aerodynamic analysis in this study.

The range of AoA used in the study is -3° to 9° and the lift-to-drag ratio (L/D) is estimated to analyze the aerodynamic efficiency of the aircraft. The use of Reynolds Averaged Navier Stokes (RANS) approach is used to complement the AoA and the computational expenses. The qualitative results are obtained for skin friction (C_f) and pressure (C_p) distribution to understand the salient flow features on and around the aircraft body, respectively. The obtained results comply well with the existing literature and follow the trends available w.r.t the entire aircraft simulations. However, the lack of validation due to the unavailability of the experimental data for this particular aircraft is a limitation of the study.

Based on the study, it can be concluded that the RANS CFD model created for the detailed aerodynamic performance analysis performed well and provided fruitful results. Modular automation using scheme files for volume mesh generation and solver setup was achieved in the methodology that reduced manual efforts and errors. The concerned geometric features such as multi-planform wing, T-tail configuration, inverted horizontal stabilizer, etc showed good aerodynamic characteristics and complemented aerodynamic forces on the aircraft body. The aerodynamic efficiency (L/D) for the selected range of AoA showed good results and trends.

Acronyms

AoA Angle of Attack. 1, 8, 9, 11, 12, 14, 19, 21

AR Aspect Ratio. 2

BOI Body of Influence. 6

CAD Computer-Aided Design. 1, 3, 4, 6

CFD Computational Fluid Dynamics. 1–3, 6, 10, 11, 19–21

GCI Grid Convergence Index. 10, 11, 19

MAC Mean Aerodynamic Chord. 4

MRF Multiple Reference Frames. 3

PID Property ID. 6

RANS Reynolds Averaged Navier Stokes. 1, 2, 8, 9, 19, 21

RANS Unsteady Reynolds Averaged Navier Stokes. 2, 9

RC Remote Controlled. 1, 20, 21

SA Spalart-Allamaras. 9

SAE Society of Automotive Engineers. 1

SIMPLE Semi-Implicit Method for Pressure Linked Equations. 10

SRS Scale Revolving Simulations. 2, 9

SST Shear Stress Transport. 9, 21

TSST Transition Shear Stress Transport. 9

Symbols

| Symbol | Description | Units |
|---------------|---------------------------------------------|-------------------|
| S_{ref} | Reference Area | [m^2] |
| α | Angle of Attack (AoA) | [<i>degree</i>] |
| α_{cr} | Critical Angle of Attack (AoA) | [<i>degree</i>] |
| L | Characteristics Length | [m] |
| M | Mach Number | [$-$] |
| R_e | Reynolds Number | [$-$] |
| C_p | Pressure Coefficient | [$-$] |
| C_f | Skin Friction Coefficient | [$-$] |
| L/D | Lift to drag ratio (Aerodynamic Efficiency) | [$-$] |

Contents

| | | |
|----------|-----------------------------------------------------------|-----------|
| 1 | Introduction | 1 |
| 1.1 | Background | 1 |
| 1.2 | Aim | 1 |
| 2 | Methodology | 3 |
| 2.1 | Pre-Processing | 3 |
| 2.1.1 | CAD Cleaning | 3 |
| 2.1.2 | Domain Creation | 4 |
| 2.1.3 | Surface Meshing | 5 |
| 2.1.4 | Volume Meshing | 6 |
| 2.2 | Solution Approach | 8 |
| 2.2.1 | Solver Settings | 8 |
| 2.2.2 | Boundary Conditions | 9 |
| 2.2.3 | Discretization schemes and convergence criteria | 10 |
| 2.2.4 | Mesh Verification | 10 |
| 2.2.5 | Validation | 11 |
| 2.3 | Post-Processing | 11 |
| 3 | Results | 12 |
| 4 | Discussion | 19 |
| 5 | Conclusion | 21 |
| 6 | Appendix | 23 |

1 Introduction

1.1 Background

The development of a product such as an aircraft requires strong planning, established methodologies, and meeting milestone deadlines. The aircraft that is analyzed in this study started from hand-drawn sketches on paper, refined in the aircraft conceptual design phases using the established methodologies [1] and [2]. The purpose of this aircraft was to participate in the SAE competition in Brazil with an aim of completing the mission profile with an incremental payload with successive flights. The methodology helped in the development of a tool in the conceptual design phase that could transform the design requirements into detailed geometric and design parameters for further development of a detailed 3D CAD model of the aircraft. Preliminary analysis performed for aerodynamic performance (airfoil, drag estimation, altitude influence, etc) and structural strength helped to refine salient geometric features.

Converting the conceptual design i.e. the detailed CAD model to actual aircraft is the prototype realization phase. The aircraft was manufactured using various materials and 3D-printed components highly coupled with the SAE requirements and regulations. The aircraft had 3 test flights, resulting in crash landings with pilot feedback of instability and tail rotation. Therefore, any investigative study is required to understand the aerodynamic performance of the entire aircraft using CFD as the re-manufacturing of an aircraft and flight testing is expensive and unfeasible.

1.2 Aim

The present study focuses on the aerodynamic analysis of the entire aircraft using industry-standard tools and approaches. Immense investment and research in the field of CFD have made it possible today to simulate the flow over an entire road vehicle, aircraft, sky-scraping buildings, an entire urban area, and much more. The need for CFD is inevitable as the construction and experimental testing of a product (e.g. aircraft) is an iterative process that may require certain changes after each iteration. There are numerous possible changes during the conceptual design phase which reduces as the product development matures. The availability of powerful computation resources at hand is one of the fundamental requirements to perform these scientific studies. The computational costs for these CFD analyses are much smaller when compared to the experimental setups required for the same which involves site construction, customized equipment, replication of flow conditions, etc.

The validation of benchmark cases using CFD solvers has been the strength of CFD software and serves as the unit cell in many practical and larger-scale industrial scenarios. However, the problem of performing the simulation for an entire aircraft, urban area, etc is still associated with approximations and simplifications at geometric and flow condition levels. This results in deviations from the experimental studies where the design limitations are mitigated using the miniature models but the boundary conditions are very specific and associated costs are huge. This leads to the CFD approaches at the cost of computational resources, where the difficulties associated with high-quality grid generation and mesh verification can be

mitigated by following the best practices available for grid generation, turbulence model selection as per the flow physics, RANS, Unsteady Reynolds Averaged Navier Stokes (RANS) or Scale Revolving Simulations (SRS) approaches depending on the requirements, etc.

The holistic aim is to conduct the CFD analysis of the aircraft model to estimate the aerodynamic efficiency (L/D) [3] by following the best practices [4]. The L/D is inversely proportional to the energy required by the aircraft and is also influenced by C_D , C_L , α , and Aspect Ratio (AR) which are very important parameters for an aircraft[3]. It also becomes an important parameter to predict the payload capacity of the aircraft in level flight. The parametric nature of the study promotes the steady state RANS approach which further limits the angle of attack below the critical angle ($\alpha < \alpha_{cr}$) of the wing (airfoil S1223) which is discussed later in the report.

2 Methodology

The CFD models consist of geometric simplifications and assumptions for flow physics which leads to various errors like discretization errors [5], residual convergence issues due to uncleaned CAD models or solver setting, validation deviations due to certain assumptions, etc. Hence, the selection of methodology becomes crucial to minimize the associated errors and represent the intended flow physics.

2.1 Pre-Processing

This section explains the pre-processing stages from CAD cleaning to volume meshing. The details CAD design of the RC aircraft with the payload Fig. 1 is good from a design and presentation point of view but possesses several challenges for external solve CFD model like sharp edges, undesirable internal (batteries, wires) and external (propeller, motor, screws) components. Hence, cleaning the CAD model is crucial for geometric simplifications and better simulation convergence.

2.1.1 CAD Cleaning

The CAD cleaning is a crucial part of the entire analysis process and should be done with great planning to mitigate potential geometric, discretization, and convergence issues in the later stages. The cleaning is also associated with flow physics i.e. internal or external, overall aim of the study, etc. The salient features of the external flow around an aircraft are the main focus of the present study for which internal components and detailed outer components are undesirable to simplify the meshing process. The details of removed components and modification are presented below:

- 1 **Propeller and motor:** The entire flow physics changes with the association of the propeller which involves rotation, and unsteady turbulent flow. The position of the propeller and motor at the aircraft nose makes the flow turbulent and requires significant meshing generation cost. Hence, removed during the cleaning process, and recommended to be analyzed exclusively using Multiple Reference Frames (MRF) or sliding meshing approaches [6] [7].
- 2 **Internal components:** The payload that is housed in the fuselage, batteries, wiring, ribs, stringers, spars, etc are the integral parts of the aircraft. These parts are important for avionics, structural strength, joining fuselage and wings, etc but least important for external aerodynamics of the aircraft. Hence, removed and updated with surfaces in the required region.
- 3 **Component Connection:** This implies the connection regions such as wing-fuselage join, boom tube connection with the fuselage and vertical stabilizer, etc. During manufacturing, these regions have fillets with varying radii for better flow distribution leading to a reduction of interference drag component. However, in CAD creation the detailing is generalized with sharp joints leading to meshing difficulties and convergence issues.

4 Sharp Edges: The uncleaned CAD model had many sharp edges at the wing trailing edge, component attachment regions, landing gear, boom tube, etc which are converted to round edges to ease the surface mesh generation process and better element growth during volume meshing. The sharp edges e.g. at the wing trailing edge also important for fluid flow and resolving high gradients in the wing wake [4].

5 Control Surfaces: For trimming and stability control surfaces play a vital role. Their main purpose is served with the deflection angle and the working is better captured with step response approaches e.g. Simulink. These are removed (rudder and stabilizer) and updated to fixed surfaces (ailerons).

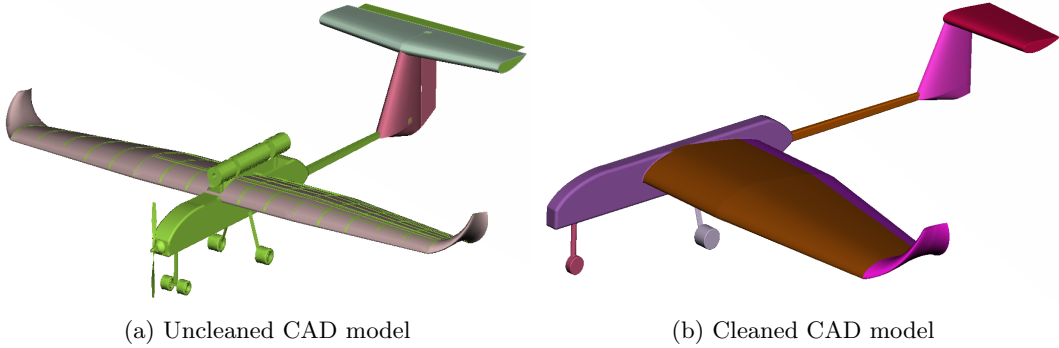


Figure 1: The cleaned RC aircraft model with applied geometric symmetry

After cleaning the CAD model, the next is to check the entire geometry for intersections and proximity checks readily available in ANSA. The topology of all the curves has to be corrected i.e. all the curves should be yellow and undesirable curves (red and cyan) should be rectified [8]. A good practice with cleaning in ANSA is to remove all the unnecessary points, and curves and only keep the required parts which aid in surface meshing and export of the mesh.

2.1.2 Domain Creation

The domain creation is vital in external flow dynamics with appropriate sizing to establish the flow from the inlet to the model and eliminate the influence of boundary conditions from the outlet and sides on the model. The domain size is generally based on a characteristic length associated with the model e.g. Mean Aerodynamic Chord (MAC) of the wing or longitudinal length (L) of the aircraft. For the present study, longitudinal length (L) is used. The recommendations for 2D and 3D domain size are different where domain size $> 40L$ is recommended for 2D and $25L - 50L$ for 3D in all directions from the model. This is because the disturbances reduce slower in 2D and faster in 3D[4]. The popular shapes used for airfoil and aircraft analysis are bullet-shaped or rectangle for the ease of applying boundary conditions [4] [9]. In this study rectangular shape domain is utilized Fig. 2, to use two edges as velocity inlets and two as pressure outlets as discussed later in the report. The size of the domain from the aircraft nose in lateral (x), vertical (y), and longitudinal (z) are $30L$, $44L$, and $73L$ respectively in all three directions.

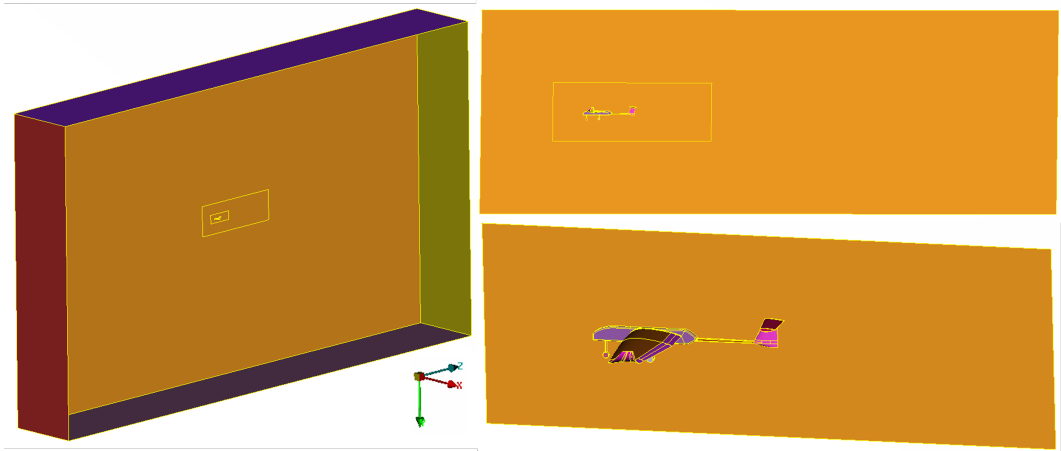


Figure 2: Symmetric domain with inner (right bottom) & outer (right top) BOIs

2.1.3 Surface Meshing

Good surface meshing is vital for the creation of high-quality volume mesh. As shown in Fig. 3, the refinement of critical regions is important as the gradients are high and need to be resolved to capture the salient features of the flow.

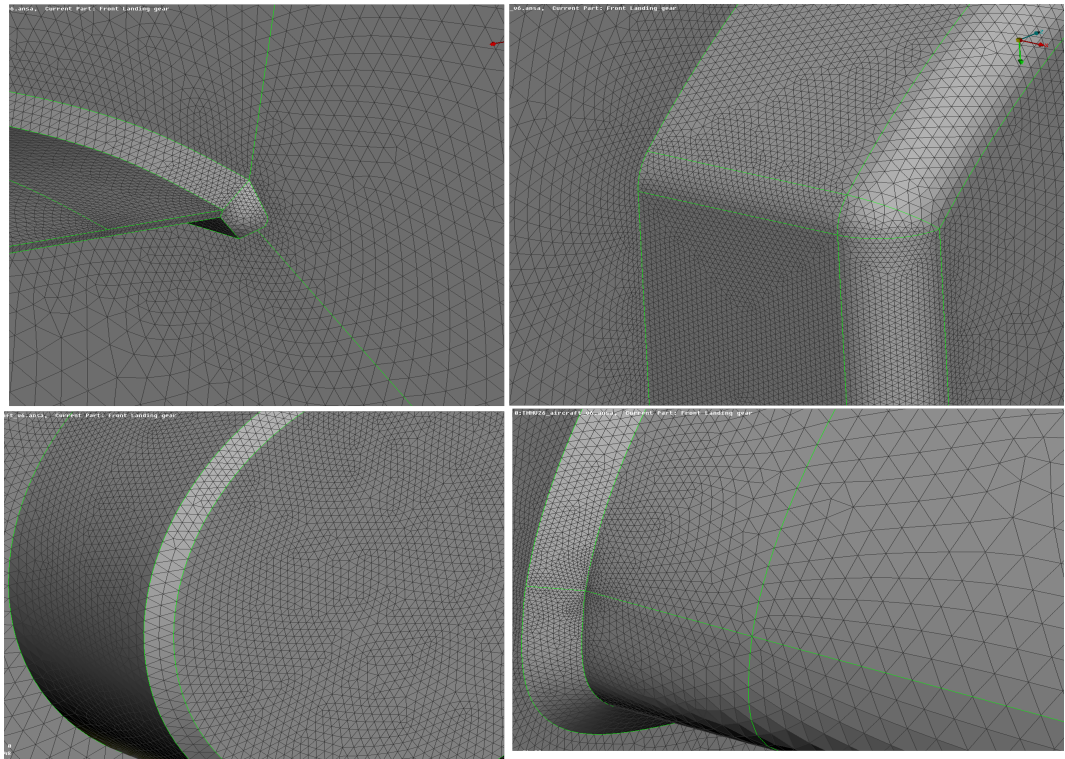


Figure 3: Surface meshing, trailing edge - fuselage (left top), front landing gear wheel (left bottom), fuselage nose (right top) and wing leading edge (right bottom)

In ANSA, the first step is to identify various surfaces/regions e.g. landing, wing, fuselage, etc, and register each as the Property ID (PID) ([8]). This eases the visualization and handling of parts during CAD cleaning and meshing, and later applying boundary conditions in the solution stage. The next, step is surface meshing for which two algorithms are utilized Adv. Front and CFD [8]. The Adv.Front generates uniform surface mesh as the cost of more elements, whereas the CFD algorithm generates a high-quality surface mesh i.e. refined according to the local curvature. However, tends to generate large elements over the smooth planar surface which adversely affects the aspect ratio.

Therefore, Adv.Front is used for large planar surfaces e.g. fuselage front and landing gear for uniformity, whereas CFD algorithm for local refinements such as wing leading edge, trailing edge, component interfaces Fig. 3. The triangular elements are selected for surface meshing instead of quad or tria/quad combination to better capture the complex curvatures, and local refinement and eventually aid in the creation of prism (inflation) layers during volume meshing in Fluent.

The surfaces are created with the default conformal mesh which results in pyramid elements in the volume mesh at the intersection. A non-conformal approach (interface elements not aligned) is also supported in ANSA which will prevent pyramid elements in volume mesh and is more robust [10]. However, the flux transfer across the non-conformal element faces is calculated between the overlapping zones by creating additional sub-division on the faces associated with interpolation errors [6].

The general procedure is to activate one PID at a time, mesh it, check and improve the mesh quality, and freeze it. The mesh quality is based on the Fluent criteria for which standard element skewness (0.5), and $\min(30^\circ) - \max(1.7 * 60^\circ)$ angle for tria and quad elements. In Fluent maximum skewness recommended is 0.95 i.e. 95 % and the angles to be closer to 60° [6]. The poor-quality elements are referred to as off elements must be fixed using the improve option under meshing. For a PID, when off elements are fixed, its surface mesh can be frozen and the next can be activated. The frozen PID mesh is not affected by the mesh of other PID and thus becomes a useful tool to generate good quality mesh faster.

Once, the surface mesh is generated on the aircraft and the domain, it is exported as a Fluent-compatible mesh file (.msh). Two Body of Influence (BOI) are created for the present problem to have a better transition of element growth away from the aircraft model and locally refine the region around the aircraft to resolve the high flow gradients. A rudimentary surface mesh is also created on BOI and exported (.msh) which are utilized as geometric regions for refinement during volume meshing.

2.1.4 Volume Meshing

The volume mesh for this study is generated in Ansys Fluent using a scheme file (.scm) that automates the entire process of volume mesh generation and quality improvement. Many mesh element types can be used to fill the domain volume like tetrahedron, hexcore, polyhedron or poly-hexcore [6]. Each element type has associated merits and demerits that are discussed in this section as mesh generation time can significantly influence the deliverable timelines.

Initially, tetrahedron elements are used as the mesh generation time is the lowest, and estimation of first layer height is important to achieve the intended $y+$ for the corresponding turbulence model. Once, the first layer height is fetched, hex-core mesh is used as it gives higher quality mesh for lesser elements compared to tetra mesh. The mesh generation time is more but it is a good trade-off for the quality. Each element of hex-core mesh has 6 faces meaning more neighboring cells and improved flux averaging leading to better accuracy and parallel meshing [6]. However, the no. of elements could significantly increase between coarse, medium, and fine mesh for verification. Poly mesh solves the issue of the number of elements by significantly reducing it, suitable for complex geometry, and more neighboring cells. However, mesh generation time is the highest among all mesh types, especially for finer meshes [6]. To get the benefit of faster mesh generation and better quality of the poly mesh, Fluent also has the option of poly-hexacore Fig. 4 5. It tries to create a hexahedral dominant bulk which is also suitable for complex geometry and the rest of the domain is filled with poly elements. The parallel meshing of hexacore is also applicable, thereby reducing mesh generation time.

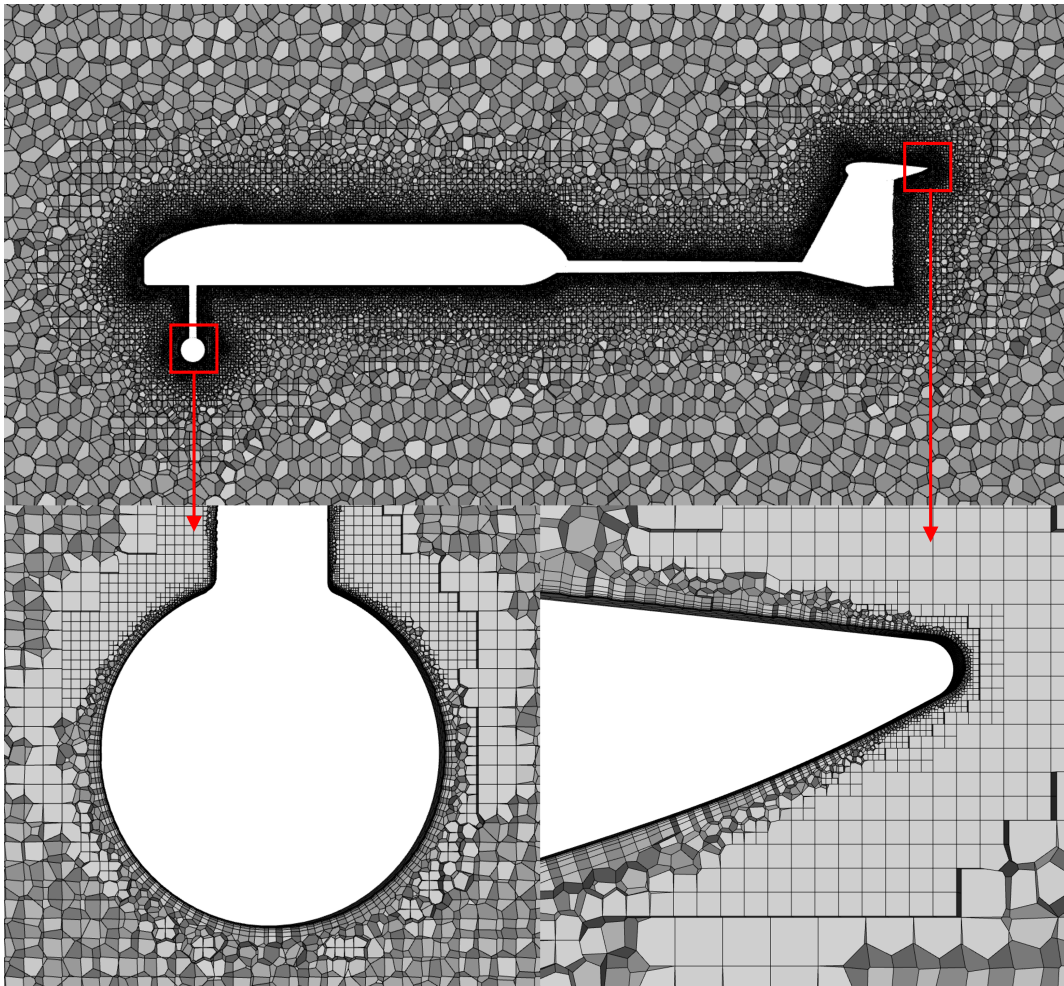


Figure 4: Element growth around front landing gear and horizontal stabilizer

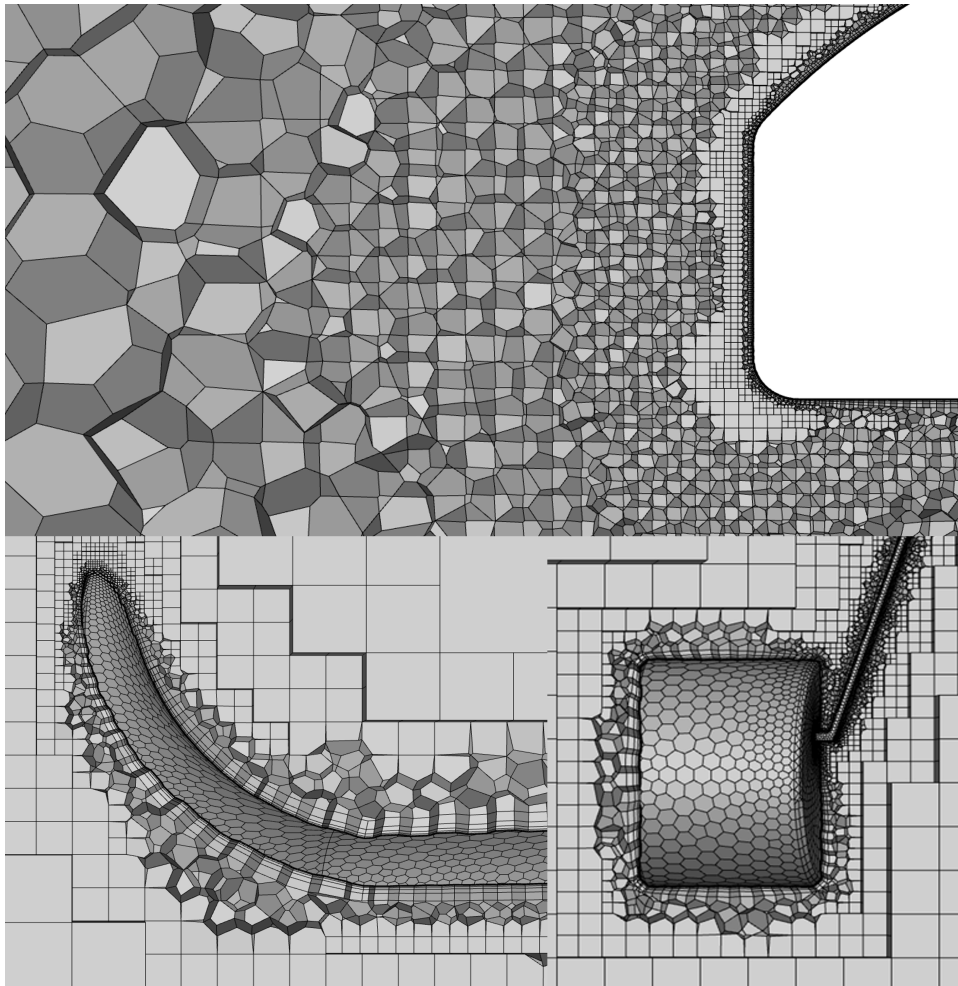


Figure 5: Element growth around fuselage front, landing gear, and winglet

2.2 Solution Approach

2.2.1 Solver Settings

The study is performed for multiple AoA in the range [-3, -1.5, 0, 1.5, 3, 6, 9] and for simplification of flow physics AoA (α) ≥ 9 are not considered as the flow becomes unsteady and separation occurs for AoA closer to stall angle ($\alpha_{cr} = 14$). The phenomena like massive wake and vortex shedding become dominant and limit the ability of RANS models [11]. The flow velocity is 8.531 m/s implying $M = 0.025$ which is considered as an incompressible flow region [12] as the density changes are smaller than 5%. This motivates the use of a Pressure-based segregated solver [6]. The solver results in better turnaround time and 1.5 to 2 times lower memory consumption than the density-based solver [4].

The parametric nature of the study with multiple $\alpha < \alpha_{cr}$ and the $R_e = 2.9e^5$ in the turbulent flow regime [12], the primary focus is on resolving the mean solve. This promotes steady RANS simulations to predict C_d , C_l , and L/D values. RANS is avoided due to its computational heaviness that gets amplified due to the mesh verification process and AoA range. For the SRS models, the mesh verification can be done on 1 mesh by iteratively improving it to a required resolution which would dictate the result accuracy but also involves computational and verification costs [11]. The RANS and SRS could be preferred if fewer AoA or a particular flow feature is the area of interest or the deliverable time for a parametric study is more.

The 1st consideration for the turbulence model is $k - \omega$ Shear Stress Transport (SST) that has proven superior performance for boundary layer separation and adverse pressure gradients, especially for lower Reynolds numbers [4] [6] observed close to the wall surface. The initial $k - \omega$ model showed boundary layer sensitivity towards ω , in turn making it sensitive towards free stream boundary conditions which is then mitigated for in $k - \omega$ SST [4]. Another consideration was Transition Shear Stress Transport (TSST), the R_e for the present study is close to the transition turbulent regime, hence TSST model becomes the 2nd consideration. The TSST model solves additional two equations for intermittency (γ) and Transition R_e ($R_{e_{\theta,t}}$) compared to the SST model. The calculation of γ allows us to predict the transition by setting $\gamma = 0$ in the laminar boundary layer, $\gamma = 1$ in the fully turbulent boundary layer, and $0 < \gamma < 1$ in the transition zone. This tells the percentage of time that the turbulent fluctuations are present in the boundary layer. The critical momentum thickness R_e ($R_{e_{\theta,c}}$) where the intermittency first starts to increase and the transition zone length both are empirically related to ($R_{e_{\theta,t}}$) [13]. Another model worth mentioning is the Spalart-Allamaras (SA) model, which is recommended for 2D problems with attached flow, but not recommended for 3D flows with strong separation and free shear flows [4]. Eventually, the SST model was selected with the area-weighted average of $2 < y+ < 7$. The continuous development of the SST model makes it robust and reliable.

2.2.2 Boundary Conditions

A square domain is selected for the present study, allowing the aircraft model to be stationary inside the domain and eliminating the need for rotation and re-meshing for each AoA. The varying α is accounted for in the velocity components at the inlet boundary condition. Velocity Inlet condition is applied on two sides (front and bottom) with a velocity magnitude same as the conceptual design phase i.e. 8.531 m/s ($R_e = 2.9 * 10^5$). A pressure outlet with zero gauge pressure is applied on the other two boundaries (back and top). The aircraft body is assigned with no-slip wall condition and symmetry for the plane of geometric and flow symmetry. The symmetric condition enforces zero flux on all quantities across the symmetric boundary, the normal velocity component is zero. No diffusion flux across leads to normal gradients being zero. Since zero shear is present, it acts as a slip wall in viscous flows [6]. However, only the normal component of turbulent kinetic energy is zero which could influence the domain flow even when the side boundary is sufficiently far from the model. Therefore, a free slip wall condition is applied on the side boundary.

2.2.3 Discretization schemes and convergence criteria

The pressure velocity-coupling and the discretization schemes are important as they dictate the result accuracy and residual convergence. In the study, Semi-Implicit Method for Pressure Linked Equations (SIMPLE) and Coupled schemes were tested for pressure-velocity coupling where SIMPLE is based on a predictor-corrector approach (segregated) and Coupled solves continuity & momentum equations together [6].

The coupled scheme with second-order spatial discretization for pressure, momentum, and turbulent quantities is recommended [4] for its robustness for steady-state flows and superior performance compared to segregated schemes [6]. However, the present study encountered convergence issues for continuity and momentum residual, output parameters (L/D , wall shear stress, moment), and reversed flow on the pressure outlet boundaries. To mitigate the issues and achieve smooth convergence, the higher-order relaxation and successive decrement of the pseudo time scale factor (from 1 to 0.2) were also employed which temporarily suppressed the fluctuations. Another recommended measure is to change the under-relaxation for pressure (from 0.5 to 0.3) and velocity (from 0.5 to 0.7) [4] which unfortunately did not mitigate the convergence issues. The scheme was then switched to SIMPLE with second-order spatial discretization. The residual convergence was smooth and without any fluctuations. However, the convergence was slow and required more iteration compared to the Coupled scheme.

The 2nd upwind for spatial discretization gives higher-order accuracy [4] [6]. The gradient estimation uses the least square cell-based method [6]. The least square method accuracy is good and is comparable to the method with the highest accuracy (Green-Gauss node-based) and is also comparatively less computationally expensive [6]. The residual convergence of $< 10^{-3}$ was achieved but is insufficient to conclude that the solution is converged. Therefore, parameters like L/D , wall shear stress, and pitching moment about the quarter chord are also observed till convergence. The component-wise convergence of L/D is important and was also observed as components like landing gear and wake flow show oscillatory behavior [4].

2.2.4 Mesh Verification

The discretization error quantification from the study is essential to convey to the reader that the simulation model is sufficiently good. The main sources of errors in the simulation model are mesh resolution, discretization, mesh quality, and associated simplifications and assumptions in modeling. The Grid Convergence Index (GCI) method is used in this study which is based on the Richardson Extrapolation method for the estimation of discretization error [5] suitable for monotonic convergence as seen in this study [14]. The method is well-accepted within the CFD community and has been evaluated over hundreds of CFD cases over the years [5]. The grid size (h) can be understood as the characteristic length of any element in the grid and the grid refinement factor (r) is recommended to be $>= 1.3$, the value for (r) is not deduced using formal derivation but instead, it is based on the experience of CFD community [5].

$$D = F_y * \sin(\alpha) + F_z * \cos(\alpha), \quad L = F_y * \cos(\alpha) - F_z * \sin(\alpha) \quad (1)$$

Table 2: Mesh Verification details

| Mesh | Elements | h | r | $L/D_{\alpha=9}$ | $GCI_{L/D} \%$ |
|--------|---------------|---------------|------|------------------|----------------|
| Coarse | $8.83 * 10^6$ | $3.51 * 10^2$ | - | 4.19 | - |
| Medium | $19.4 * 10^6$ | $2.70 * 10^2$ | 1.31 | 4.22 | 0.15 |
| Fine | $43.4 * 10^6$ | $2.07 * 10^2$ | 1.33 | 4.42 | 1.01 |

The details of mesh verification are based on an important parameter for an aircraft i.e. lift-to-drag ratio (L/D), Table. 2. The L/D is estimated at $\alpha = 9^\circ$ which is the highest α value in this study. The axial (F_z) and vertical (F_y) forces were resolved into components parallel and perpendicular to the free-stream flow direction to calculate the drag and lift forces using (Eq. 1). The mesh verification shows that both medium and fine meshes have $GCI < 5\%$ which is an accepted uncertainty value for CFD simulations [14]. Hence, the medium mesh is used for further analysis of the entire range of AoA as the GCI value is very low, with smoother convergence than coarse mesh, and less computation time than fine mesh.

2.2.5 Validation

The experimental data for the aircraft used in this study is not available for validation purposes. Therefore, the lack of validation leads to the comparison of obtained results against the trends in available literature in the form of textbooks, research articles, online blogs, etc. The history of the aviation sector is immense, and the contribution from CFD simulations, benchmark studies, and ongoing research in the field of turbulence modeling have strengthened the literature. The validation of the present study is limited to L/D ratio trends, C_p and C_f distribution on the aircraft body, and the C_p distribution around the aircraft.

2.3 Post-Processing

The contours and results presented in this study are obtained in Paraview v5.12 which is an open-source software used for the post-processing of small-large volumes of data. The qualitative visualization and presentation aid in comprehending the simulation results which also gives rise to the development of powerful tools like Paraview with automation capabilities. The automation aspect is becoming crucial in the new software to minimize human error, faster results, significantly improve deliverable time, etc. In Paraview, users can use the trace functionality in which user-performed manual steps are traced, and an automation script written in Python (programming language) is automatically generated. Another approach is to write the Python script using the Paraview-provided Python libraries/packages which can be made more robust and dynamic, but this approach requires a decent amount of programming knowledge. In the present study, another approach is utilized in which all the parent and child nodes are created manually in Paraview for one dataset1, and a state file (.pvsm) is created for the same. For dataset2, this state file is loaded in Paraview, and in the parent node dataset2 was read instead of dataset1 and the new results are reflected in all the children nodes. This approach saves creation time of children nodes for each data set, but also involves manual intervention for reading data and saving images.

3 Results

The results presented primarily focus on the pressure coefficient (C_p) Fig. 6 and skin friction coefficient (C_f) Fig. 7 distribution on the aircraft body, C_p plots around the aircraft on several longitudinal Fig. 9, lateral Fig. 8, and vertical Fig. 10 planes to visualize in the 3D space around the aircraft. The comparison is shown between $\alpha = 9^\circ$ and $\alpha = -3^\circ$ which are the highest and the lowest AoA values used in this study. Towards the section end, L/D variation with α are shown in Fig. 11

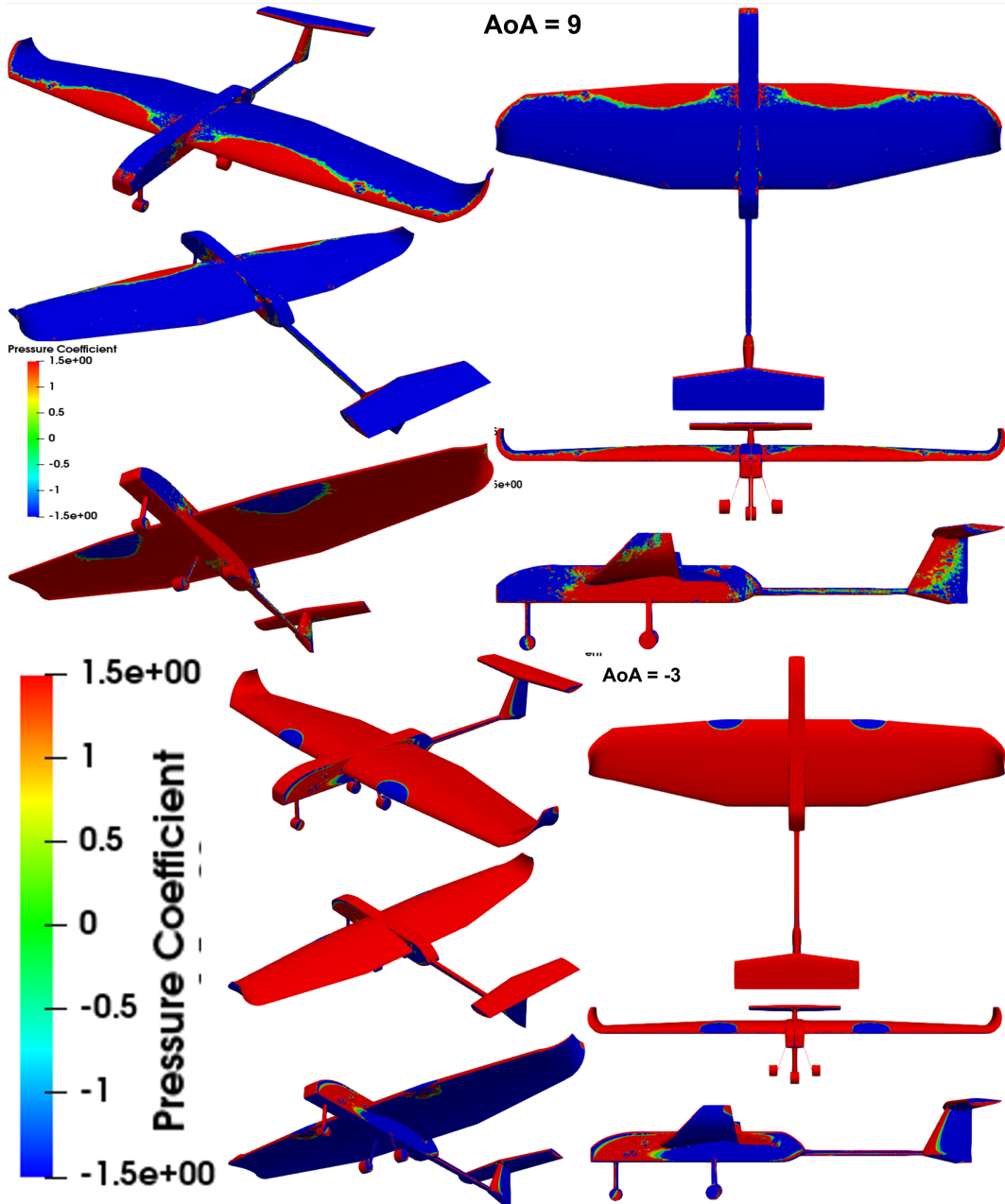


Figure 6: C_p distribution comparison between $\alpha = 9^\circ$ and $\alpha = -3^\circ$

Fig. 6 shows C_p distribution on the aircraft body. For $\alpha = 9^\circ$ the highest (+) C_p values are observed on the bottom surface of the wing and all other components as well. The high C_p distribution is also seen on the leading edge of the rectangular section of the wing, fuselage front face, front and rear landing gears, and the vertical stabilizer leading edge. Whereas, the lowest (-) C_p values are distributed on top surfaces like top wing and winglets, horizontal stabilizer, boom tube, trailing edge of the vertical stabilizer, and small regions of rectangular-trapezoidal wing interface.

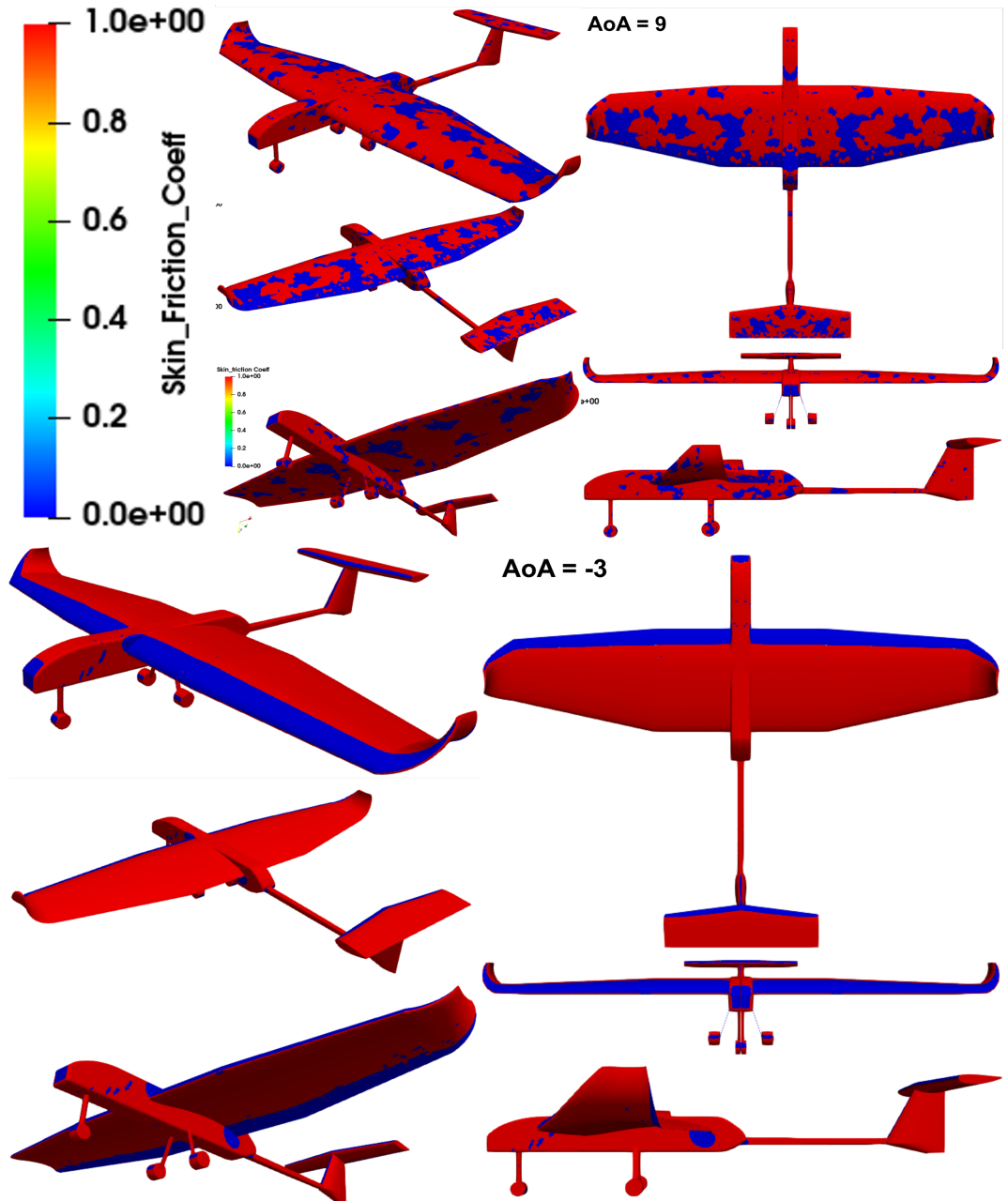


Figure 7: C_f distribution comparison between $\alpha = 9^\circ$ and $\alpha = -3^\circ$

For $\alpha = -3^\circ$, the opposite trends are seen for C_p distribution compared to $\alpha = 9^\circ$, the $+C_p$ values are observed on the top surfaces, and $-C_p$ on the bottom surfaces. Significant regions of the vertical stabilizer and the rear landing gear show $-C_p$ distribution, along with the rectangular-trapezoidal wing interface, Fig. 6.

The C_p distribution on the wing and the horizontal stabilizer is similar for both $\alpha = 9^\circ$ and $\alpha = -3^\circ$. The transition between $+C_p$ and $-C_p$ for high AoA ($\alpha = 9^\circ$) is not smooth as seen for ($\alpha = -3^\circ$) on the wing surface, fuselage side & bottom faces, vertical stabilizer, boom tube, and winglet bottom surface.

For both AoA, the landing gear front and side surfaces, and side faces of the horizontal stabilizer show the rapid transition between $+C_p$ and $-C_p$. On careful examination, small patches of high $+C_p$ are observed on the wing trailing edge and the wing-fuselage interface for $\alpha = 9^\circ$.

The C_f distribution (Fig. 7) is estimated based on the wall shear component along the longitudinal axis of the aircraft ($z_{\text{wall_shear}}$) to signify flow attachment on the surfaces. The C_f distribution for high AoA ($\alpha = 9^\circ$) is not smooth on the entire aircraft. It has the highest values bottom and side surfaces wing, winglet, fuselage horizontal and vertical stabilizer, boom tube, and landing gears.

Significant regions with the highest C_f are observed on the top surfaces of the wing (near the leading edge) and horizontal stabilizer as well. At $\alpha = -3^\circ$, negligible non-uniformity in C_f distribution is seen on the fuselage and lower surface of the wing (trailing edge), but overall the distribution is uniform compared to $\alpha = 9^\circ$. Contrary to $\alpha = 9^\circ$, at $\alpha = -3^\circ$ the leading edge (top) and trailing edge (bottom) surfaces, front fuselage face, and the leading edge of the horizontal stabilizer show the least C_f value. All other surfaces at $\alpha = -3^\circ$ show high C_f value, Fig. 7.

Fig. 8, shows C_p distribution comparison in the % span(b) longitudinal planes. For $\alpha = 9^\circ$, the low-pressure region ($-C_p$) is well distributed above the longitudinal axes, except near the winglet. For $x \in [0b, 0.087b]$ show high $+C_p$ at boom-tail interface and the entire downstream of the tail is low pressure ($-C_p$) region. At the rect-trap wing transition and bottom face of the horizontal stabilizer leading edge, a small high $+C_p$ region is observed $x = 0.35b$. At the winglet, the C_p distribution is similar to the tail, but the $-C_p$ and $+C_p$ regions are almost equal, and on a closer look small bubble of $-C_p$ are seen on the bottom winglet surface, Fig. 8. At $\alpha = -3^\circ$ and $x = 0b$ and $x = 0.35b$ (rect-trap wing transition), the small counter C_p regions are observed close to the front fuselage, front landing gear, and on the wing leading edge region. Near the winglet, the $+C_p$ is significantly bigger than the $-C_p$.

Fig. 9 shows C_p distribution comparison on the longitudinal planes. At the wing leading edge ($z = -1$) for $\alpha = 9^\circ$, two high $+C_p$ regions are observed on the upper surface near the rect-trap wing interface, just below these regions of $-C_p$ are present. On the upper surface, a very small set of high $+C_p$ regions are observed at the wing-fuselage interface and near the winglets.

The $-C_p$ and $+C_p$ are well distributed (0.5c) downstream on the wing ($z = -0.75$) and around the winglet. On the boom tube ($z = -0.25$ and $z = 0$), the $-C_p$ region reduces and moves towards the $+C_p$, but as the horizontal stabilizer approaches $-C_p$ increases again and on the stabilizer ($z = 0.25$) the $-C_p$ is similar to the 0.5c wing. However, below the stabilizer, the presence of a vertical stabilizer divides the $+C_p$ regions into three, Fig. 9. The high $+C_p$ regions are observed on the wing ($z = -1$) for $\alpha = -3^\circ$ as well but on the lower surface. At the 0.5c

($z = -0.75$) downstream on the wing, small $-C_p$ regions are observed on the upper surface near the winglets but the overall C_p is well distributed.

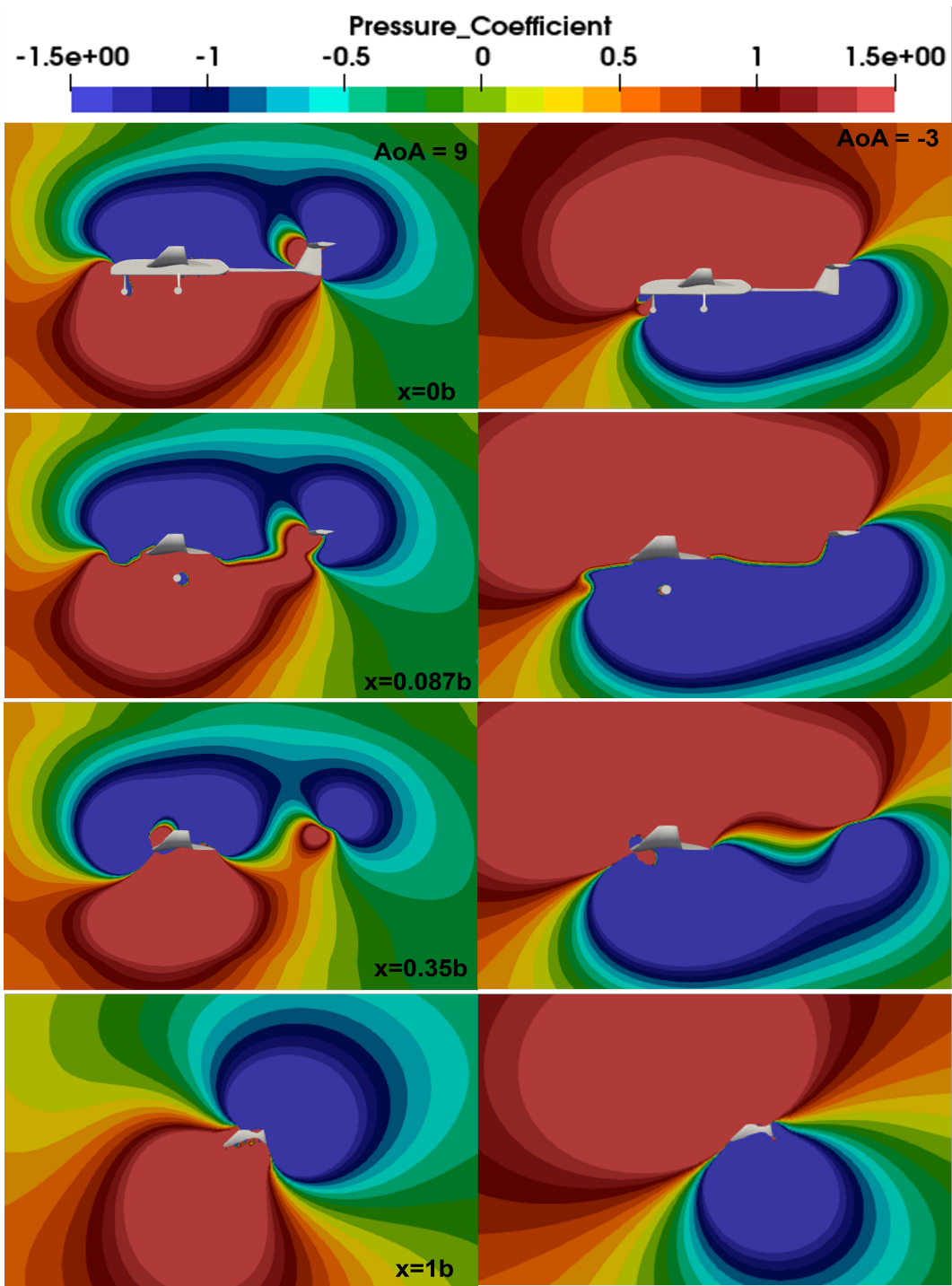


Figure 8: C_p distribution comparison between $\alpha = 9^\circ$ and $\alpha = -3^\circ$ on various lateral planes along the % span (b)

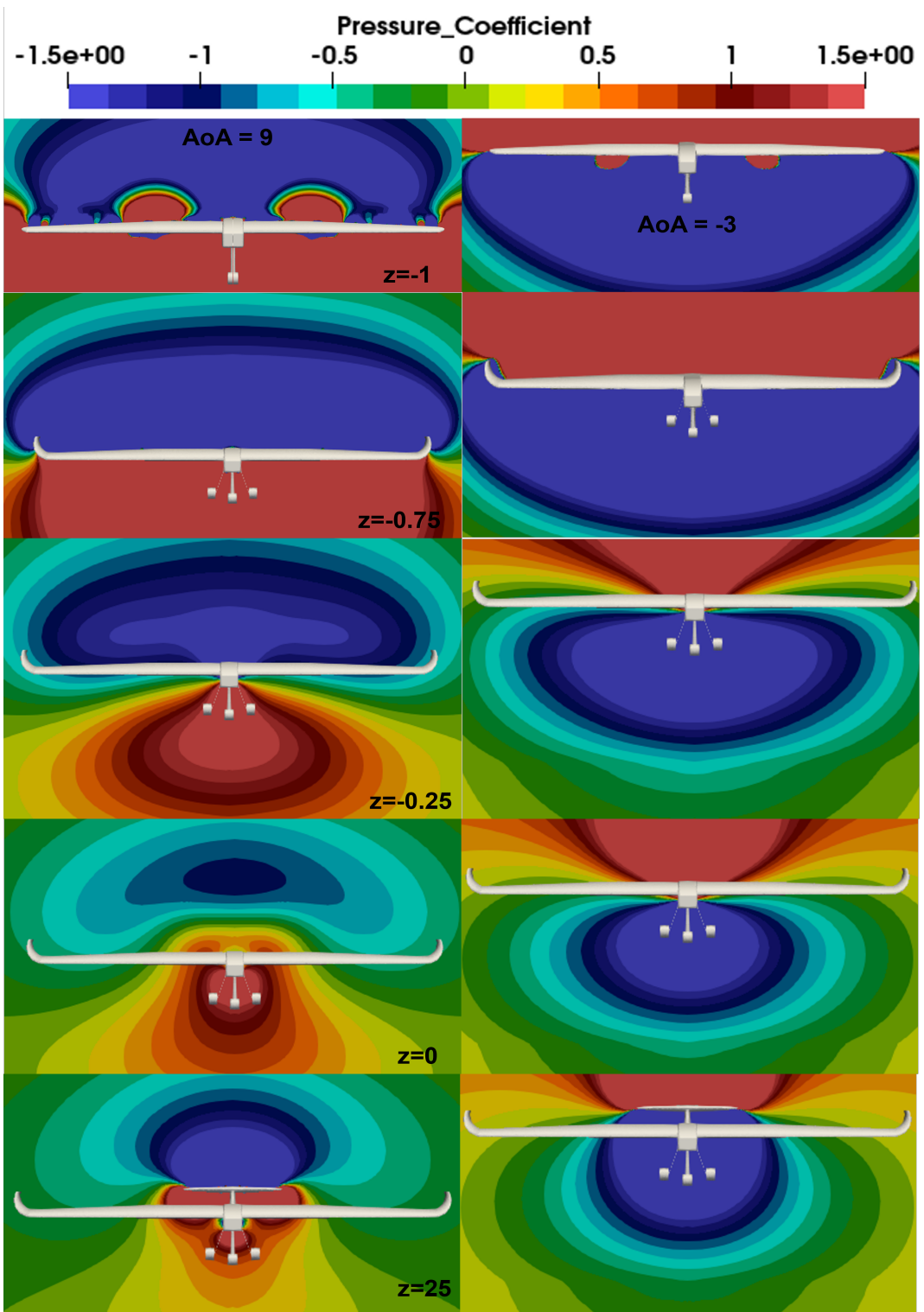


Figure 9: C_p distribution comparison between $\alpha = 9^\circ$ and $\alpha = -3^\circ$ on various longitudinal planes along the fuselage length

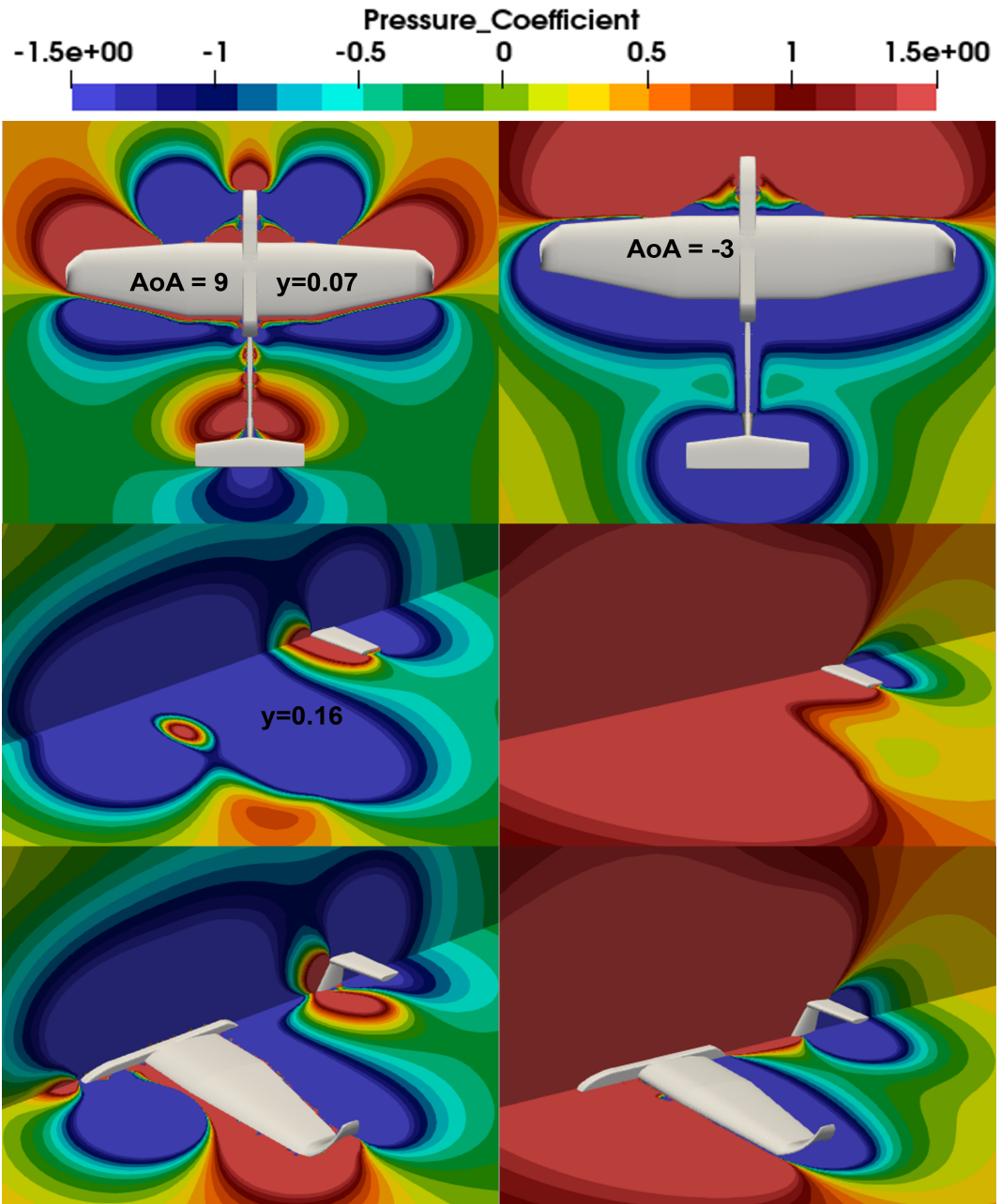


Figure 10: C_p comparison between $\alpha = 9^\circ$ & $\alpha = -3^\circ$ on various vertical planes

Vertical plane C_p distribution is captured in Fig. 10. For $\alpha = 9^\circ$ at $y = 0.07$, the high $+C_p$ regions are observed in front of the fuselage front, wing-fuselage interface, leading edge of the trapezoidal wing, the small region along the boom tube, and significant high $+C_p$ region at the boom-vertical stabilizer interface. On the other hand for $\alpha = -3^\circ$, the high $+C_p$ region is only present upstream to the wing leading edge. downstream the entire aircraft is surrounded by the $-C_p$ region, Fig. 10. At the $y = 0.16$ for $\alpha = 9^\circ$, a high $+C_p$ region is present at the rect-trap wing interface and upstream for the horizontal stabilizer leading edge.

The L/D against the α plot is shown in Fig. 11, where the approx value of maximum $L/D = 14.6$ is achieved at $\alpha = 0.3^\circ$ and minimum $L/D = -10.8$ at $\alpha = -1.75^\circ$. As the α increases, the L/D gradually decreases 5.55 at $\alpha = 6^\circ$. From $0 \leq \alpha \leq 3$, the L/D remains between 5-13. However, at $\alpha = 6^\circ$ a sharp decrement is observed $L/D = -10.1$, then steadily increases to -7.98 at $\alpha = -3^\circ$.

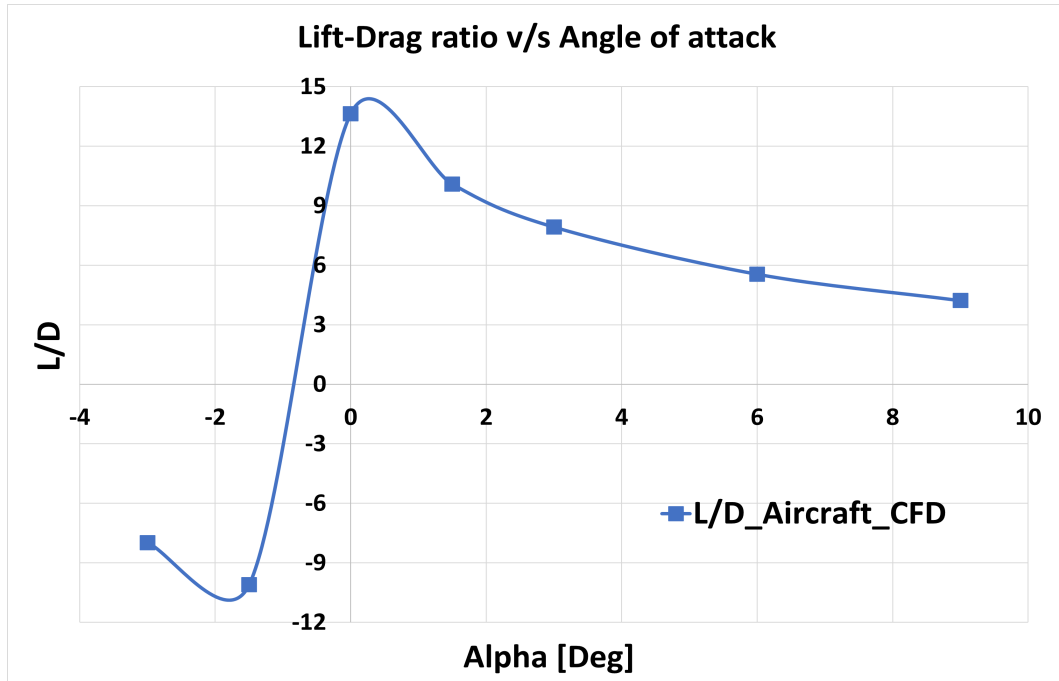


Figure 11: L/D ratio variation with α for the entire aircraft

4 Discussion

The verification (Table. 2) methodology [5] [14] followed in the present study is well accepted in the CFD community for performing RANS studies with monotonic convergence of residual [14]. However, the GCI value should also be seen from the perspective of the aim of the study e.g. there could exist a large difference in the order of magnitude for 1% or 5% GCI for steady-state analysis focused on spatial/grid resolution.

A complete validation on the other hand can only be performed if the entire study replicates the experiment in terms of boundary conditions and strictly follows the non-dimensionality of flow parameters which still would require certain assumptions in the experiment and simulation setup. Since the present study lacks the experiment data of the same or similar aircraft, the results are validated against the well-established literature trends. For a complete validation, both simulation and experimental uncertainties are to be quantified [14], unlike verification where only simulation uncertainties are estimated.

The $-C_p$ regions observed on the lower wing surface for $\alpha = 9^\circ$ and upper surface for $\alpha = -3^\circ$ at the planform transition from rectangular to trapezoidal wing imply the phenomenon of leading-edge suction [1]. This reduced pressure exerts a suction force in the focused region in the forward direction [1]. The phenomenon is desired to counter the drag component and the favorable conditions for its occurrence are high α , large leading-edge radius, and wing sweep (here rect-trap planform transition). The leading edge radius and sweep have a powerful influence on the suction force and are well fulfilled by the wing at the observed region. The Semi-Tapered planform of the wing allows for better C_p distribution outboard by reducing the stagnation condition at the wing leading edge (regions of $+C_p$). It increases the section lift coefficient [2] which is seen in Fig. 6 as the $-C_p$ distribution on the entire trapezoidal (outboard wing) at $\alpha = 9^\circ$. However, the associated drawback of construction complexity was tackled by making it detachable and modular.

The skin friction coefficient C_f as mentioned earlier is based on the z_wall_shear component (along fuselage length in $+z$ direction). For $\alpha = 9^\circ$, the blue region ($C_f = 0$) implies the flow separation or region of re-circulation which on the wing upper surface is near the trailing edge at the wing planform transition and near the winglets which are prone to vortex format and flow reversal, Fig. 7. The trailing edge of the wing and the horizontal stabilizer at high α on the upper wing surface show the same trend as the flow becomes turbulent (usually the point of maximum airfoil thickness i.e. 20% of chord for S1223) and due to adverse pressure flow reversal occurs leading to wake formation [1]. For $\alpha = -3^\circ$ to lowest C_f are observed at the leading edge on the upper wing surface and trailing edge on the lower surface as at $-\alpha$ the flow tends to separate on the lower wing surface near the trailing edge. At both α , the re-circulation ($C_f = 0$) is also seen near the interface of wing-fuselage at the trailing edge where the wake effects and interference drag are high Fig. 7.

The C_p distribution shown in Fig. 9, 8 and 10 for both AoA well captured the regions of high and low pressure (C_p), especially on the wing and horizontal stabilizer upper surfaces, implying a good lift distribution for semi-tapered planform wing with high-wing configuration as well as around the blended winglets, Fig.9.

The effectiveness of the winglets can be seen from the lack of high $+C_p$ regions in the form of wing tip vortices leading to high lift-induced drag and promote attach flow [2], Fig. 9. The combination of the inverted horizontal stabilizer and the T-tail configuration has a desired nose-down pitching moment on the aircraft as the C_p distribution on the inverted wing is similar to that of the main wing, Fig. 9, 10. The $-C_p$ distribution on the upper surface of the inverted stabilizer resulted in the attached flow implied by the C_p and C_f distribution at $\alpha = 9^\circ$. However, the configuration is susceptible to deep stall and hence lost pitching controls [1], [2].

The parameter of huge importance for an aircraft (L/D) is a direct measure of the aerodynamic efficiency of the aircraft's design [1]. The results shown in Fig. 11 are in close agreement with the existing trends and magnitude available in the literature [2] and the study performed for blended wing body unmanned aerial vehicle [15]. The CFD results were validated against the wind tunnel test conducted for the scaled-down (1/4) prototype of the aircraft in the study [15]. The peak L/D value is observed at small α and gradually decreases as α tends to α_{cr} . The sharp decline in L/D ($\alpha < 0^\circ$ leading to $L/D < 0$) Fig. 11, is due to the re-distribution of the pressure where low pressure ($-C_p$) region comes below the aircraft Fig. 8 results in negative lift. The high L/D value is also important for the low thrust and energy requirement [3] of the aircraft for the same travel distance which becomes important for an RC aircraft.

5 Conclusion

The CFD analysis of the RC aircraft using the RANS approach and following the corresponding best practices is performed in the present study for various α . The primary objectives were to investigate the distribution of C_p , C_f , and L/D to highlight the salient geometric design points and corresponding flow behavior. The aerodynamic efficiency of the RC aircraft design is also studied as the function of α . Based on the analysis, the following conclusions are drawn:

- The proposed methodology with the combination of automation scheme files significantly reduces the manual effort and deliverable time for a parametric study.
- The poly-hexcore volume meshing is recommended to capture the complex geometry and curvature near the aircraft body and the overall accuracy of the results.
- The S1223 airfoil selected for the wing provides high aerodynamic efficiency (L/D) for the RC aircraft for a good range of AoA.
- The k– ω SST turbulence model is recommended to obtain C_p and C_f distribution at high $+\alpha$ ($< \alpha_{cr}$) and small $-\alpha$ which agree well with existing literature and the flow physics.
- The maximum $L/D = 14.6$ is achieved at $\alpha = 0.3^\circ$ and minimum $L/D = -10.8$ at $\alpha = -1.75.3^\circ$ for the aircraft.
- The Semi-Tapered wing design promotes the desired lead edge suction force and better C_p distribution on the outboard wing.
- The blended winglet design promotes attached spanwise flow and prevention of wing-tip vortices and hence reduces lift-induced drag.
- The fuselage design and high-wing configuration are well suited for C_p and C_f distribution on the upper surfaces.
- The combination of the inverted horizontal stabilizer and the T-tail configuration produces a similar C_p distribution as on the main wing, promoting strong up-lift and thus nose-down pitching moment.

References

- [1] Raymer DP. Aircraft design: a conceptual approach. AIAA Education series; 1992.
- [2] Gudmundsson S. General aviation aircraft design: Applied Methods and Procedures. Butterworth-Heinemann; 2013.
- [3] Lift-to-drag ratio. Wikipedia;. Available from: https://en.wikipedia.org/wiki/Lift-to-drag_ratio.
- [4] Falk Gotten MMCB Dr Felix Finger. A review of guidelines and best practices for subsonic aerodynamic simulations using RANS CFD. 2019.
- [5] et al IBC. Procedure for Estimation and Reporting of Uncertainty Due to Discretization in CFD Applications. 2008.
- [6] Ansys. Ansys Fluent Theory Guide. 2020.
- [7] Ferenc Szlivka GFIM Csaba Heteyi. Comparison of Mixing Plane, Frozen Rotor, and Sliding Mesh Methods on a Counter-Rotating Dual-Rotor Wind Turbine. International Journal of Multiphase Flow. 5/08/2023. Available from: <https://doi.org/10.3390/app13158982>.
- [8] v 15 x Tutorials A. THE BASICS GEOMETRY CLEANUP AND SHELL MESHING. BETA CAE Systems S.A;. Available from: http://dma.ing.uniroma1.it/users/paciorri/the_basics_cfd.pdf.
- [9] Idealsimulations. CFD Computational Domain. Idealsimulations;. Available from: <https://www.idealsimulations.com/resources/cfd-computational-domain/>.
- [10] Systems BC. ANSA version 20 1 .x User Guide. 2019.
- [11] Menter FR. Best Practice: Scale-Resolving Simulations in ANSYS CFD. 2015.
- [12] Vesteeg HK, Malalasekera W. An Introduction to Computational Fluid Dynamics. 4th ed. Pearson Education LTD; 2007.
- [13] Transport Equations for the Transition SST Model;. Available from: <https://www.afs.enea.it/project/neptunius/docs/fluent/html/th/node74.htm>.
- [14] Fred Stern HWC Robert V Wilson, Paterson EG. VERIFICATION AND VALIDATION OF CFD SIMULATIONS. 1999.
- [15] Mohd Saad, Nornashiha, Wisnoe, Wirachman, Mohd Nasir, Rizal Effendy, Mohd Ali, Zurriati, Askari, Ehan Sabah Shukri. Aerodynamic Analysis of Blended Wing Body - Unmanned Aerial Vehicle (BWB-UAV) Equipped with Horizontal Stabilizers. MATEC Web Conf. 2019;256:02004. Available from: <https://doi.org/10.1051/matecconf/201925602004>.

6 Appendix

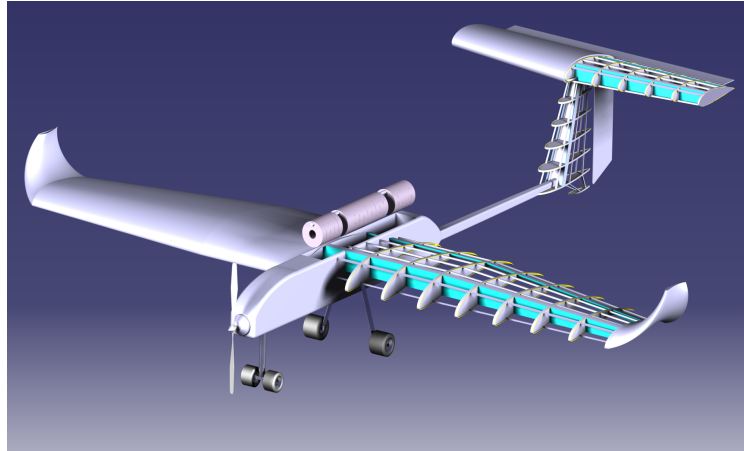


Figure 12: Conceptual design phase: Detailed CAD model



Figure 13: Product Realization: Assembled frame of the aircraft



Figure 14: Flight Test: Assembling the components before flight test